

# Spectral-temporal-spatial customization via modulating multimodal nonlinear pulse propagation

Tong Qiu<sup>1†</sup>, Honghao Cao<sup>1†</sup>, Kunzan Liu<sup>1</sup>, Li-Yu Yu<sup>1</sup>, Manuel Levy<sup>2</sup>, Eva Lendaro<sup>2</sup>, Fan Wang<sup>2</sup> and Sixian You<sup>1\*</sup>

<sup>1</sup>Department of Electrical Engineering and Computer Science, Massachusetts Institute of Technology, Cambridge, MA, USA.

<sup>2</sup>Department of Brain and Cognitive Sciences, Massachusetts Institute of Technology, Cambridge, MA, USA.

\*Corresponding author(s). E-mail(s): [sixian@mit.edu](mailto:sixian@mit.edu);

†These authors contributed equally to this work.

## Abstract

Multimode fibers (MMFs) have recently reemerged as attractive avenues for nonlinear effects due to their high-dimensional spatiotemporal nonlinear dynamics and scalability for high power. High-brightness MMF sources with effective control of the nonlinear processes would offer new possibilities for a wide range of applications from high-power fiber lasers, to bioimaging and chemical sensing, and to novel physics phenomena. Here we present a simple yet effective way of controlling nonlinear effects at high peak power levels: by leveraging not only the spatial but also the temporal degrees of freedom of the multimodal nonlinear pulse propagation in step-index MMFs using a programmable fiber shaper. This method represents the first method that enables modulation and optimization of multimodal nonlinear pulse propagation, achieving high tunability and broadband high peak power. Its potential as a nonlinear imaging source is further demonstrated by applying the MMF source to multiphoton microscopy, where widely tunable two-photon and three-photon imaging is achieved with adaptive optimization. These demonstrations highlight the effectiveness of directly modulating multimodal nonlinear pulse propagation to enhance the high-dimensional customization and optimize the high spectral brightness of MMF output. These advancements provide new possibilities for technology advances in nonlinear optics, bioimaging, spectroscopy, optical computing, and material processing.

# 1 Introduction

Multimode fibers (MMFs) have become renewed focuses of interest for investigating multimode nonlinear optics, owing to their versatile degrees of freedom for guided waves and their potential for high power scalability (1–12). Over the last 5–10 years, significant progress has been made in studying and controlling nonlinear effects in MMFs, presenting unprecedented opportunities for a plethora of applications in optical sensing, imaging, manipulation, and computing. For example, the application of MMFs to fiber lasers could permit the development of low-cost light sources with dramatically higher pulse energy and average power due to the larger mode areas of the MMFs (13–16). More importantly, the rich spatiotemporal dynamics and complex intermodal interactions in MMFs constitute a broad avenue for controlling nonlinear wave propagation, opening up possibilities for novel physics and new applications such as spatiotemporal light control (17, 18), nonlinear frequency generation (4, 12, 19–21), nonlinear optical imaging and sensing (22–25), optical wave turbulence (26–29), and optical computing (30, 31).

Recently, control of the multimode spatiotemporal light fields has been demonstrated by adjusting the input wavefront to graded-index (GRIN) MMFs for selective mode excitation (11, 15, 32–36). These studies, by exploiting the spatial degree of control of the input field, demonstrated the unprecedented potential of MMFs as technological solutions for tunable high-power light sources and spatiotemporal avenues for fundamental nonlinear optical physics. However, the primary focus on spatial control in GRIN MMFs often subjects the spatiotemporal pulses to limited capabilities in many applications due to two major problems: difficulty in control and limited broadband spectral brightness. Fiber sources with higher-dimensional tunability and broadband spectral brightness could usher in a wave of opportunities for new types of light sources and nonlinear phenomena (9, 37–43), and ignite advances in cutting-edge applications, such as bioimaging, laser manufacturing, chemical sensing, and optical computing. To realize this potential, harnessing the untapped potential of temporal degrees of freedom to control nonlinear effects in MMFs at high peak power levels presents a compelling solution.

Here we introduce a new way of controlling multimodal nonlinear effects in high-power regimes by exploiting not only the spatial but also the temporal degrees of freedom. Complementary to manipulating the input pulses that seed the nonlinear pulse propagation, we propose to modulate the multimodal nonlinear pulse propagation processes by introducing programmable time-dependent disorders along the fiber (26), which is implemented as axial-position-dependent macro-bending. This was made possible by using a single 3D-printed modulating device dubbed *fiber shaper* (conceptually depicted in Fig. 1a). By applying the fiber shaper to a standard silica step-index (SI) fiber at high-power levels (Fig. 1b), we showed effective modulation of the multimodal nonlinear pulse propagation and customization of the MMF output field in the spectral, temporal, and spatial domains.

We further demonstrated the ability to generate high peak power even extending outside the conventional soliton regime. The broadband high peak power (approaching megawatt on average) was accomplished by combining spectral energy reallocation (up to 166-fold) and temporal shortening (up to 4-fold). Such capabilities are uniquely enabled by the fiber shaper, a single all-fiber modulator without the need for external wavefront or pulse shaping. To showcase its potential, we applied the apparatus directly to multiphoton microscopy, an application with demanding needs for spectral and temporal properties of pulses. Through adaptive optimization of the fiber shaper, we achieved efficient and widely tunable two-photon and three-photon microscopy of fluorescent beads and label-free tissues. Our proposed approach, which presents the first method enabling simultaneous access to the spatial and temporal degrees of control of multimodal nonlinear effects, relies on the application of precisely controlled multi-point macro-bending to the fiber. Recent demonstrations have shown the use of piezoelectric actuators (i.e., *fiber pianos*) to induce controllable bends in MMFs for modulating modal dynamics in the linear regime (44–47). Inspired by this design, we want to develop a module that’s compatible with nonlinear regime and overcomes the challenge of tunability and low spectral brightness in fiber sources. Despite the promising applications in linear and quantum regimes (46–48), it is challenging to directly adopt linear fiber pianos to the nonlinear regime due to application-specific issues such as light loss, design flexibility, and scalability. By employing the slip-on fiber shaper created through 3D printing that supports smooth (minimal micro-bending) but large-curvature bending (sufficient modal coupling effects), we envision its potential as an accessible and flexible tool for both linear and nonlinear modulations of MMFs, with significant implications in nonlinear optics, bioimaging, and spectroscopy.

## 2 Results

### 2.1 Experimental setup

Ultrashort pulses (Light Conversion Cronus-3P) were launched into a standard silica SI MMF with a length of 30 cm by weakly focusing (see Methods). To explore the fiber shaper’s capability in both the normal and anomalous dispersion regimes, we initiated the experiments with a pump wavelength of 1300 nm (46 fs). Due to its proximity to the zero-dispersion wavelength of silica, a wide array of nonlinear effects can be effectively excited, including self-phase modulation (SPM), cross-phase modulation (XPM), four-wave mixing (FWM), multimode soliton formation, and dispersive wave emission (49–52). The fiber was mounted on a 3D-printed programmable fiber shaper that introduces multi-point macro-bending to the MMF through five individually controlled motorized actuators (Fig. 2). Each actuator locally and precisely applies controlled bending on the fiber at multiple axially dispersed positions. By producing local index perturbations, the actuators cause energy coupling between modes (53, 54) at multiple time points of the pulse evolution. When operated

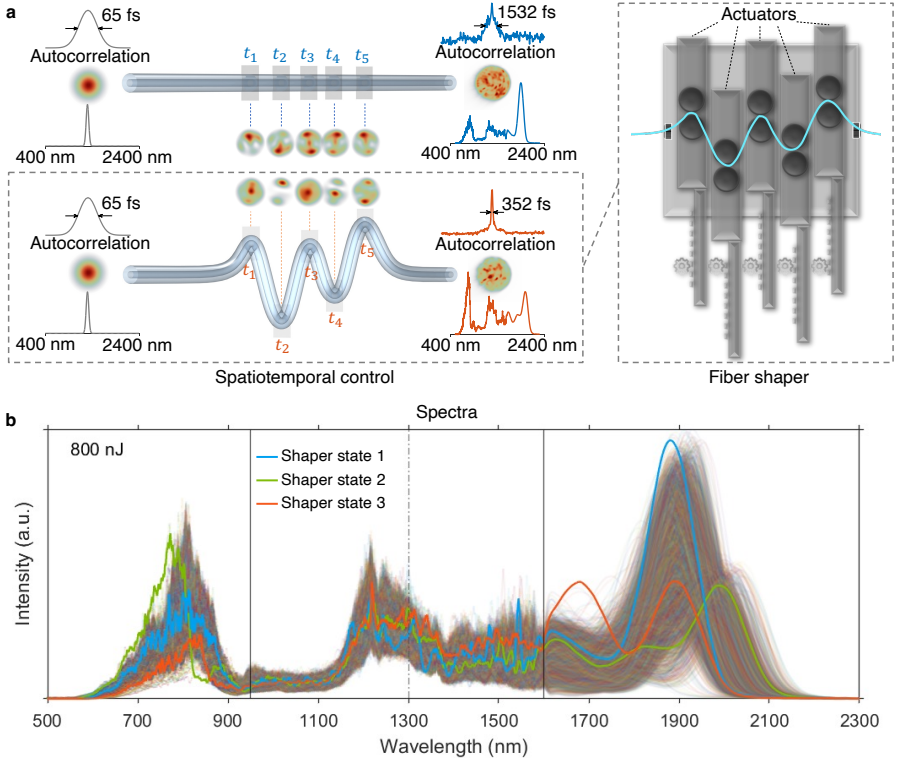


**Fig. 1 Conceptual demonstration of spatiotemporal control of nonlinear pulse propagation in MMFs by a fiber shaper.** **a**, Illustration of the principle of spatiotemporal control of multimodal nonlinear effects in MMFs by introducing programmable time-dependent disorders using a fiber shaper. The fiber shaper applies multi-point macro-bending of various bending radii to the fiber and thus alters the multimodal spatial interactions at different time points (e.g.,  $t_1$  to  $t_5$ ) along the pulse temporal evolution. **b**, Visualization of experimentally acquired output spectra of an SI MMF with the same launching condition but different combinations of actuator positions. A total of 3125 configurations were exhaustively searched, involving 5 actuators, each with 5 different states. Three representative spectra corresponding to three randomly chosen configurations are highlighted in distinct colors. Vertical solid lines mark the spectral range measured by different spectrometers. The dash-dotted line denotes the input wavelength.

together, these actuators exert the high-dimensional spatiotemporal control of the multimodal nonlinear pulse propagation, thus creating opportunities for simultaneous customization of the spectral, spatial, and temporal profiles of the fiber output pulses. Besides the ease of construction and operation, the fiber shaper maintains high light throughput with negligible transmission loss regardless of the actuator configurations, measured at  $\pm 1\%$  at high power levels (input pulse energy of 800 nJ, 85% coupling efficiency at initial states).

To understand the multimodal compositions of the spatiotemporal nonlinear effects in the SI MMF, the fiber output was spatially profiled with

multiple spectral bands of interest (see Fig. 7). The wavelength-dependent spatial profiles of the fiber output indicate that the lower-order modes are responsible for the formation of the most red-shifted multimode soliton ( $1900\pm 100$  nm; Fig. 7b), whereas the generation of the dispersive waves ( $560\pm 5$  nm,  $725\pm 25$  nm; Fig. 7b) is dominated by the higher-order radially symmetric modes, as predicted in (50), to satisfy the intermodal phase-matching condition between one of the modes comprising the dispersive waves and another lower-order mode of the multimode soliton. The region in between (i.e., SPM, XPM, and FWM) ( $900\pm 25$  nm,  $1200\pm 5$  nm; Fig. 7b) exhibits a high degree of multimodal behavior, which could be attributed to the many degrees of freedom required to satisfy the intermodal group velocity matching and intermodal phase matching (20, 55, 56). These mechanistic studies and observations not only shed light on the underlying mechanisms of the two-octave spectral broadening, but also highlight the multimodal compositions of the spectral broadening in different dispersion regimes, which lays the foundation for the broadband tunability discussed in the following sections.

## 2.2 Effective spatiotemporal control of multimodal nonlinear effects in SI MMF

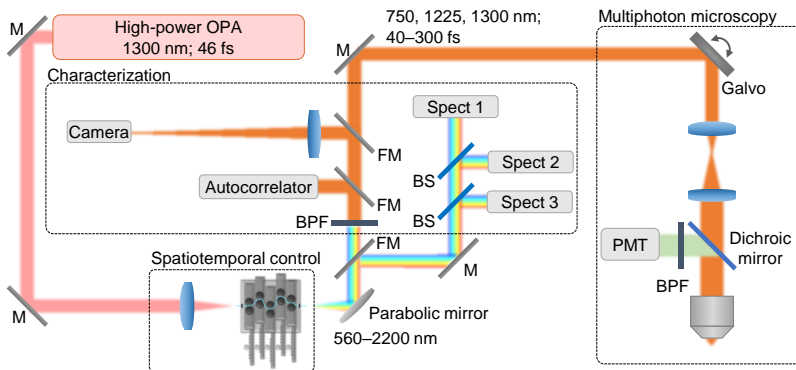


**Fig. 2 Schematic of the experimental setup.** The ultrabroadband light out of the SI MMF is collimated by an off-axis parabolic mirror before directing to the characterization apparatus and imaging system (see Methods for details). OPA: optical parametric amplifier; M: mirror; FM: flip-mirror; BPF: bandpass filter; BS: beam splitter; Spect: spectrometer; PMT: photomultiplier tube.

To achieve flexible tunability through spatiotemporal control of the multimodal nonlinear effects, we designed a fiber shaper consisting of five 3D-printed linear actuators (Fig. 3a) at a total cost of 35 US dollars including the motors and its actuators (see Methods, Section 9.2, and Figs. 10–12). The actuators can independently translate in the direction perpendicular to the optical axis. By controlling the relative shift between the actuators, macro-bending of various radii can be applied to the fiber precisely and simultaneously, allowing

for an exhaustive automated search and adaptive optimization of thousands of fiber shape configurations to achieve optimal output spectral-temporal-spatial properties. This can be readily scaled up with more actuators to unlock the full high-dimensional spatiotemporal control of the multimodal nonlinear optics (see Fig. 15). In principle, these actuators alter the local refractive index profile, causing energy coupling between modes at multiple time points during the pulse evolution, which altogether enable the high-dimensional spatiotemporal control of the multimodal nonlinear pulse propagation. This process can be modeled by supplementing the generalized multimode nonlinear Schrödinger equation (GMMNLSE) (see Methods) on the right-hand side with an additional term representing the linear mode coupling effect (55, 57, 58):

$$i \sum_n^N Q_{np} A_n(z, t), \quad (1)$$

where  $Q_{np}$  denotes the linear coupling coefficient between mode- $n$  and mode- $p$  due to a local perturbation, determined by the spatial overlap of the three quantities (see Methods);  $A_n(z, t)$  represents the temporal envelope of mode- $n$ , which is complex-valued to include the envelope phase due to distinct phase velocity of each mode (58, 59);  $z$  is the propagation direction. The modes can be simplified as the ideal modes of the unperturbed waveguide using perturbative coupled-mode theory in principle (60). However, in practice, the mode field can undergo considerable deformation in curved multimode fibers, making it necessary to consider additional variations related to mode field deformation. These variations include changes in the propagation constant and in the nonlinear coupling coefficient  $S_{plmn}^K$  and  $S_{plmn}^R$  (see Methods), which are determined by the spatial overlap between the mode- $p$ ,  $-l$ ,  $-m$ , and  $-n$ . As a result, by introducing localized changes to  $Q_{np}$  and to the mode fields at axially dispersed positions along the fiber, the spatial and temporal degrees of freedom of nonlinear pulse propagation can be simultaneously controlled.

The perturbed GMMNLSE, along with the observed evolution of the spectral broadening and spectrally distinct spatial profiles (Figs. 7 and 9), provide a key insight into the condition of effective spatiotemporal control of multimodal nonlinear optical processes in multimode fibers. At individual temporal instances, the more effectively we can modulate the linear and nonlinear mode coupling coefficients and the mode propagation constants, the higher-dimensional control and the greater tunability the source will exhibit. A lot of previous studies on multimodal nonlinear pulse propagation focused on GRIN MMFs due to their unique self-imaging properties and low modal dispersion. However, we observed that SI MMFs exhibit significantly greater tunability and higher spectral brightness under the same experimental conditions (Fig. 3b,g). This is likely due to their larger modal areas and the more closely spaced propagation constants, which collectively lead to lower peak intensity, higher sensitivity to bending, and increased susceptibility to the mode coupling effect.

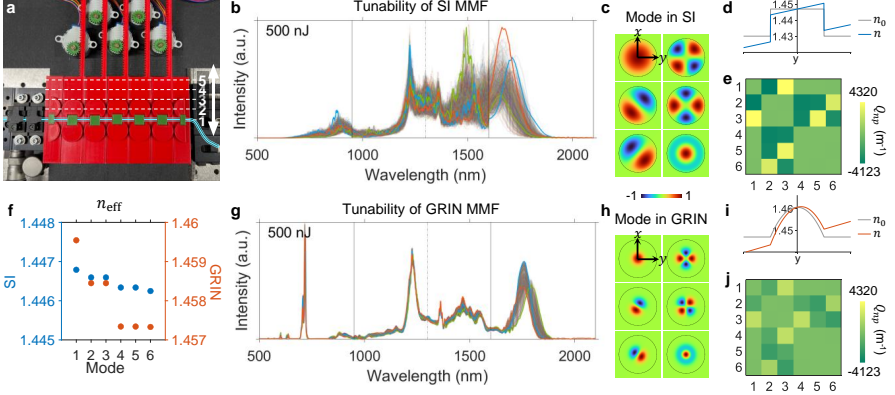


**Fig. 3 Mechanisms of spatiotemporal control of nonlinear effects in SI MMFs using fiber shaper.** **a**, Photograph of the custom-designed fiber shaper at its initial state. **b,g**, Experimental results of 30-cm-long SI MMF (50/125  $\mu\text{m}$ , 0.22 NA) (**b**) and GRIN MMF (50/125  $\mu\text{m}$ , 0.2 NA) (**g**) with the same set of macro-bending applied. Representative spectra corresponding to three randomly chosen configurations out of a pool of 3125 configurations are highlighted in distinct colors. The input pulse energy of 500 nJ is experimentally limited by the laser-induced damage to the GRIN MMF. **c,h**, Normalized electric field of the first six spatial modes in unperturbed SI MMF (**c**) and GRIN MMF (**h**), with the core-cladding interface marked in black. **d,i**, Illustrative examples of the refractive index profiles of straight ( $n_0$ ) and curved ( $n$ ) SI MMF (**d**) and GRIN MMF (**i**).  $n$  is approximately expressed by  $n_0 + n_0 y/r_b$ , where  $r_b$  represents the bend radius, which is set to 1 cm (the minimum value the fiber shaper can introduce by design). **e,j**, Linear mode coupling coefficient  $Q_{np}$  resulting from the macro-bending in **c,h** for the first six spatial modes in **b,g** in SI MMF (**e**) and GRIN MMF (**j**). **f**, Effective refractive index ( $n_{\text{eff}}$ ) for the first six spatial modes in SI and GRIN MMFs.

To gain a mechanistic understanding of this phenomenon, we simulated the effect of bending for the two fiber types using the perturbative coupled-mode theory, which assumes that the mode fields are not deformed by the weak perturbation (60). Here we present an illustrative example including the first six spatial modes, we show in Fig. 16 the 55-mode case. Figure 3c–f, h–j displays the simulation results for the SI and GRIN MMFs, showcasing the linear interactions between the first six spatial modes (Fig. 3c, h) in curved fibers (Fig. 3d, i). The resulting linear coupling coefficient is presented in Fig. 3e, j. The phase mismatch is reflected by the effective refractive index  $n_{\text{eff}}$  in Fig. 3f. Here we chose 1 cm as the bend radius in the simulation since it is the minimum value the fiber shaper can introduce by design; results including three different bending radii are displayed in Fig. 16. These simulation results show that SI MMF has a greater  $Q_{np}$  and smaller phase mismatch, both of which contribute positively to the strength of linear coupling (see Fig. 16). This indicates richer spatiotemporal dynamics can be introduced in SI MMFs with the application of macro-bending. The significantly smaller  $Q_{np}$  exhibited by GRIN MMFs can be attributed to the more confined mode field which sees weaker local perturbation at the center region (Fig. 3c, d, h, i) and hence higher resistance to mechanical deformation such as bending (61–64). Moreover, the

clustering nature of the propagation constants in GRIN MMFs makes the perturbation-induced mode coupling tend to occur between the nearly degenerate modes, commonly referred to as the degenerate-mode group (65). Both factors make the multimodal nonlinear dynamics in GRIN MMFs less sensitive to fiber bending compared to that in SI MMFs.

Apart from the tunability, we also observed that the GRIN MMFs exhibit a lower threshold for laser-induced damage. Recent work has studied the effects of damage and transmission loss induced by multiphoton absorption on GRIN and SI MMFs (66, 67). As we gradually increased the input pulse energy for the GRIN fiber, we observed a decrease in total output power and a reduction in the output spectral span, suggesting the occurrence of fiber damage. This lower damage threshold is possibly due to the parabolic index profile which leads to more severe self-focusing effects (68), and the Germanium dopant in the GRIN fiber core (69). These analyses and observations provide insights into the mechanism of fiber-shaper-based spatiotemporal control and entertain the choice of SI MMFs for a broadband high-peak-power tunable fiber source. Our observation, although unexpected, is consistent with the recent studies that show GRIN MMFs are not as sensitive to launching conditions or bending as SI MMFs (52, 62–64). Despite it being a drawback to applications that demand insensitivity to bending, the usually undesirable susceptibility to bending of SI MMFs, together with their power scalability, are essential for achieving effective spatiotemporal control of high-power pulse propagation in multimode fibers.

### 2.3 Enhanced tunability: customizing the fiber output in spectral, temporal, and spatial domains

We next evaluate the effectiveness of using fiber shaper to control nonlinear effects in SI MMFs across different dispersion regimes. This was done by examining, in distinct spectral regions, the tunability in spectral band energy (Fig. 4a,b), temporal duration (Fig. 4c), and spatial intensity profiles (Fig. 4c) of the output light field while shaping the fiber in real-time. These investigations were carried out under the same launching conditions (800 nJ, 46 fs, and 1300 nm) using the characterization apparatus depicted in Fig. 2. Figure 4a shows the spectral tunability factor across a continuous two-octave bandwidth, by exhausting the combination of actuator positions on the fiber shaper. The spectral tunability factor is defined as the ratio of the maximally enhanced intensity to the maximally suppressed intensity for each 20-nm-wide spectral band. We observed that the tunability varies substantially across the spectrum, with the minimum enhancement ratio of 3.1-fold shown in the middle of the spectral span, and significantly higher enhancement ratios ranging from 9-fold to as much as 166-fold at the two ends of the spectrum (below 800 nm and above 1500 nm). Such wavelength dependence is very likely to be the product of distinct broadening mechanisms in different dispersion regimes. To look into the versatility and effectiveness of the fiber shaper in manipulating various nonlinear effects, we next show in Fig. 4b,c representative examples in



different spectral regions, each featuring distinct dominant broadening mechanisms (see Fig. 7a). The highest spectral tunability lies in the dispersive wave regime (500–900 nm; Fig. 4b) and the soliton regime (1700–2300 nm; Fig. 4b), the 9-fold and 166-fold marked in Fig. 4a are shown as instances in Fig. 4b. A recent study observed notable differences in the spectra for multimode solitons with identical energy but different initial mode components (70), which could provide insights into the high spectral tunability within the soliton regime. Simultaneous dual-band spectral tuning, with an averaged enhancement ratio of 2.3-fold for the two bands, is exemplified for the nonlinear phase modulation regime (1000–1600 nm; Fig. 4b).

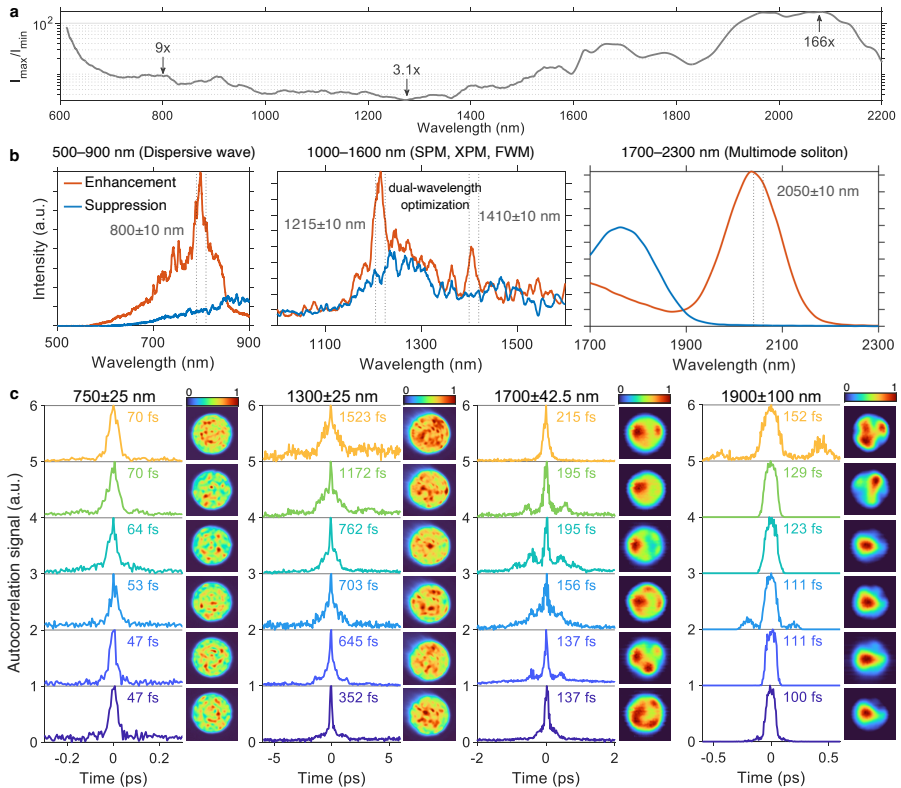


**Fig. 4 Performance of fiber shaper: customization in spectral, temporal, and spatial domains.** **a**, Ultrabroadband spectral tunability, evaluated from a set of spectra acquired from 3125 states of the fiber shaper. **b,c**, Representative examples of modulations in spectral band energy (**b**) of selected single bands and dual-band (denoted by vertical dotted lines), showing the most enhanced (Enhancement) and suppressed (Suppression) cases; and in pulse duration and the associated spatial intensity profiles (**c**) for selected spectral bands, with the center wavelength and bandwidth denoted above each panel, and the FWHM of the autocorrelation signals annotated near each panel. For visualization purposes, each intensity profile is normalized to its own maximum value.

Multimode solitons and their phase-matched dispersive waves consist of multiple mode combinations, within each combination the modes are group-velocity matched (49–52). Mechanical perturbations such as a series of macro-bending can cause major changes in the few-mode composition and thus significantly alter spectral profiles in order to re-match the group velocity via mode-dependent spectral shifting. This is also manifested by dramatic changes of the few-mode-like spatial intensity profiles of multimode solitons ( $1700\pm 42.5$  nm and  $1900\pm 100$  nm; Fig. 4c) and dispersive waves ( $750\pm 25$  nm; Fig. 4c) across seven random states of the fiber shaper. These changes reflect the capability of the fiber shaper to significantly alter the mode composition, and thus the output light field in the spectral and spatial domains. The temporal duration at the fiber output, on the other hand, shows limited tunability as solitons and dispersive waves are intrinsically nearly transform-limited pulses. In contrast, the regime dominated by SPM, XPM, and FWM are known for highly nonlinear, strongly coupled, and highly multimodal behavior. The resulting spectrum is the incoherent summation of many modes, which makes spectral shape less sensitive to modal distribution changes and reduces the effectiveness of tuning the spectral intensity. The speckled spatial intensity profile ( $1300\pm 25$ ; Fig. 4c) corroborates the highly multimode nature of the nonlinear phase modulation process, in which the many-mode composition is needed to satisfy the intermodal phase-matching and velocity-matching conditions. Interestingly, the control in the temporal domain is much more significant in the nonlinear phase modulation regime than other regimes, ranging from 1523 to 352 fs based on the full-width at half-maximum (FWHM) of the autocorrelation signals, from 1080 to 250 fs assuming a Gaussian pulse shape for simplicity. This observation can be attributed to the effective reduction of modal dispersion in the multimodal output through optimization of fiber shaper-induced linear mode coupling.

Our results demonstrate that the fiber shaper effectively manipulates the modal compositions of the propagating pulse and the resulting spectral-temporal-spatial properties of the output light field, exceeding what has been shown before. The intricate nonlinear interactions emphasize the benefits of using a fiber shaper to control the spatiotemporal dimension of the nonlinear dynamics in order to achieve a targeted output in different dispersion regimes. Earlier studies have successfully demonstrated broadband supercontinuum generation using silica MMFs in longer pulse duration regimes (8–11, 21, 71). In this work, we demonstrate a two-octave tunable source in the femtosecond regime, which enables applications in multiphoton microscopy due to its high-peak-power pulses.

## 2.4 Ultrabroadband high-peak-power tunable source for multiphoton microscopy

The results above demonstrate the potential of the fiber-shaper-controlled SI MMF for achieving an ultrabroadband high-peak-power tunable source, which

is capable of modulating the output field in the spectral, temporal, and spatial domains. This capacity can facilitate diverse applications in spectroscopy, sensing, and imaging applications. As a proof-of-concept demonstration of such potential, we directly applied the proposed source for multiphoton microscopy (MPM) (see Methods and Fig. 17) to investigate whether it can be adaptively optimized for nonlinear imaging which demands sources with high spectral brightness (5–50 nJ) (72, 73), short temporal duration (10–500 fs) (74, 75), and confined spatial profiles (76).

We first characterized the performance of the proposed source with fluorescent beads for two-photon fluorescence (2PF) and three-photon fluorescence (3PF) imaging. For comparison, we acquired reference images with a commercial laser source based on an optical parametric amplifier (OPA) from Light Conversion Cronus-3P. The results are presented in Fig. 5a–h, and the experimental setup which includes the optical path for imaging and the characterization of spectral, temporal, and spatial profiles of the fiber source, is depicted in Fig. 2. The raw output of the MMF was directed to a scanning MPM system after passing through selected bandpass filters ( $750 \pm 25$  nm for 2PF,  $1300 \pm 25$  nm and  $1225 \pm 25$  nm for 3PF). This setup can be readily improved in future studies with advanced wavelength selection mechanisms for more systematic and automatic multiband imaging. We observed that using the initial state of the fiber shaper, i.e., an unoptimized form, resulted in poor image quality (e.g. low multiphoton signals), which can be largely attributed to insufficient peak power due to the thinning of the energy distribution that comes with spectral broadening and/or temporal broadening caused by modal and chromatic dispersion.

Remarkably, by adaptively and coarsely optimizing the fiber shaper using feedback from the multiphoton signals, i.e. greedy search in our experiment, enhancements of 15-fold, 11-fold, and 6-fold in signals were achieved for 2PF (750 nm), 3PF (1300 nm), and 3PF (1225 nm) microscopy, respectively (Fig. 5c,f,h). To investigate the mechanisms of the improvement, we looked into the spectral, temporal, and spatial characteristics of the output pulses before and after optimization (Fig. 5j–r), and calculated the multiphoton signal generation efficiency according to the method described in (77) (Fig. 5s). To highlight the role of spectral and temporal tuning and for simplicity, the high-order dispersions and multimodal spatial compositions are neglected in the calculation and the pulse shape and spatial profile of the fiber source are assumed to be the same as those of the laser (see Methods and Section 9.3). The strong agreement between the measured and the calculated improvements in signals confirms that pulse energy and pulse duration are the dominant factors affecting multiphoton signal generation efficiency in our experiments. Notably, the measured and calculated signal improvements for 2PF are more closely matched than those for 3PF. This can be attributed to the fact that the generation efficiency of 2PF is less dependent on the spatial distribution of the beam compared to 3PF (77) (see Fig. 19).

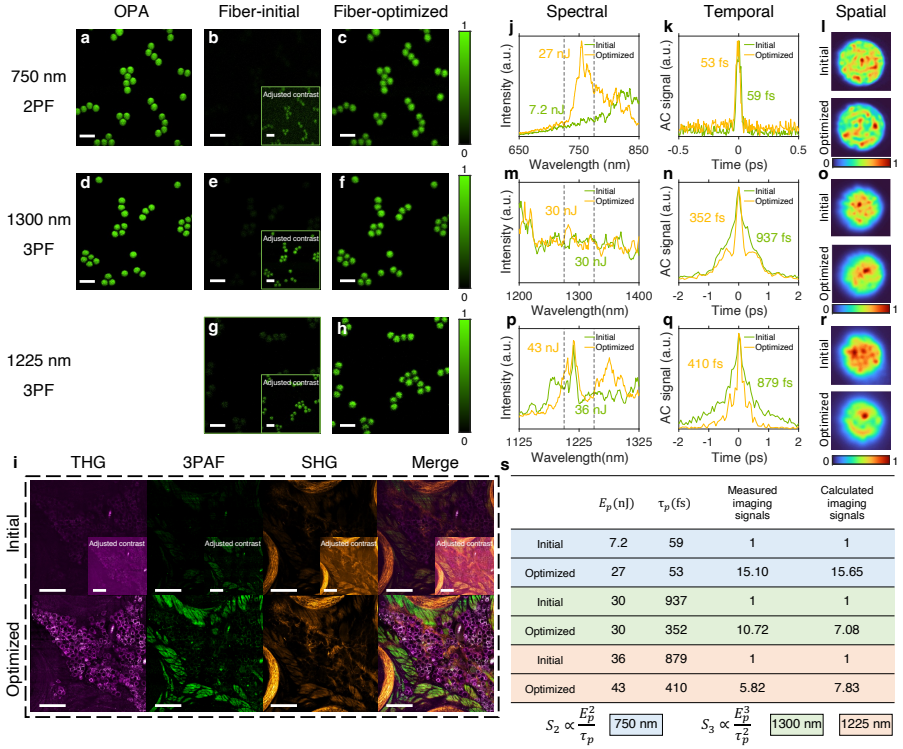


**Fig. 5 Multiphoton microscopy with the fiber-shaper-controlled MMF source.** **a–h**, Demonstration of 2PF and 3PF imaging on fluorescent beads using OPA (**a,d**), initial fiber source (**b,e,g**), and optimized fiber source (**c,f,h**). The contrasts of the insets are adjusted for visibility. Scale bars: 20  $\mu\text{m}$ . **i**, Pseudo-color presentation of label-free imaging of fixed tissue from the mouse whisker pad at 1225 nm excitation using the initial and optimized fiber source, showing THG (magenta) signals of adipocytes, 3PAF (green) signals of muscles, and SHG (yellow) signals of collagen fibers. The contrasts of the insets are adjusted for visibility. Scale bars: 200  $\mu\text{m}$ . **j–r**, Characterization of the spectral (**j,m,p**), temporal (**k,n,q**), and spatial (**l,o,r**) properties of the output beam of the initial and optimized fiber source corresponding to the images in **a–h**. The 50-nm spectral band energy and the FWHM of the autocorrelation (AC) signals are indicated in the figures. The spatial profiles are individually normalized to their maximum intensity. **s**, Validation of the signal improvement from the images compared to the theoretical values calculated from pulse measurement.

Moreover, we observed that the output field optimization for signal enhancement of 2PF and 3PF varies as a result of different underlying mechanisms. Specifically, the signal enhancement for 2PF was primarily driven by a 3.8-fold increase in the spectral intensity at 750 nm, whereas the enhancement for 3PF signals was primarily due to a 2.7-fold (at 1300 nm) and 2.1-fold (at 1225 nm) reduction in pulse duration, resulting in peak powers of 0.72, 0.12, and 0.15 MW, assuming Gaussian pulse shape. This difference is consistent with our findings presented in Fig. 4, where the tunability in spectral and temporal domains exhibits strong spectral dependence due to the distinct dominant nonlinear effects: higher spectral tunability was observed in

the dispersive regime (750 nm), whereas better temporal tunability was found in the nonlinear phase modulation regime (1300 and 1225 nm). Additionally, we observed that the corresponding spatial profile of 3PF showed a tendency to be less speckled and more confined when the pulse was shortened, due to a reduced modal dispersion. The reduction in speckling in 3PF is likely to result in less image blurring compared to 2PF (see Fig. 18).

We next examined the performance of the proposed source for label-free imaging of freshly excised mouse tissue. We selected the  $1225 \pm 25$  nm excitation band, which is not covered by most commercial high-power OPA or low-rep high-peak-power lasers. After the same procedure of optimization (greedy search based on the imaging signals), the optimized SI MMF allows the simultaneous visualization of adipocytes through third-harmonic generation (THG), muscles through three-photon autofluorescence (3PAF), and collagen fibers through second-harmonic generation (SHG) (Fig. 5i), which demonstrated the potential of this source as a widely and continuously tunable source for bioimaging.

## 2.5 Extension to other wavelengths

We have demonstrated above the effectiveness of using fiber shaper for spatiotemporal control of various nonlinear effects across different spectral regions, which leads to a high-peak-power source spanning the whole broadened spectrum. The broadened spectral span, however, exhibits strong wavelength dependence. For example, our results (see Fig. 13 show that pumping in the normal dispersion regime (e.g., 800 nm) leads to limited spectral broadening and smaller spectral tunability, while pumping deeper into the anomalous dispersion regime (e.g., 1550 nm) results in a broad but discontinuous spectrum. To obtain an efficient and wide continuum for sufficient broadband spectral brightness, one often needs to pump the waveguide in the anomalous dispersion regime close to its zero-dispersion wavelength (ZDW). For fused silica, the ZDW is close to 1280 nm. Although the main results of this study were generated using a pump wavelength of 1300 nm, the fiber shaper can be easily extended to other wavelengths - with comparable broadening and tunability - by pumping a multimode waveguide with ZDW close to the pump wavelength.

Here, to demonstrate the extension of the fiber shaper to other more accessible wavelengths such as 1040 nm, we leverage the blue-shifted ZDWs of the higher-order fiber modes to match the pump wavelength (see Fig. 14. The results are presented in Fig. 6. The upper panel shows the spectral broadening with matched ZDW by exciting the  $LP_{07}$  mode using a spatial light modulator (SLM) (78), resulting in a spectrum spanning from 550 to 1650 nm covering 1.6 optical octaves, which is comparable to the 2-octave spectral span we obtained in the previous sections. Inset shows the spectral tunability between 900–1700 nm, exhibiting great capability for spectral energy reallocation. In comparison, the reference spectrum obtained by weakly focusing without matching the pump and zero-dispersion wavelengths is displayed in the lower panel, limited spectral broadening was observed. Other methods to shift

the ZDW includes dispersion engineering and composing the waveguide with non-silica materials (21, 79–81). Through these techniques, more wavelengths can be potentially accessed with optimized spectral span and tunability.

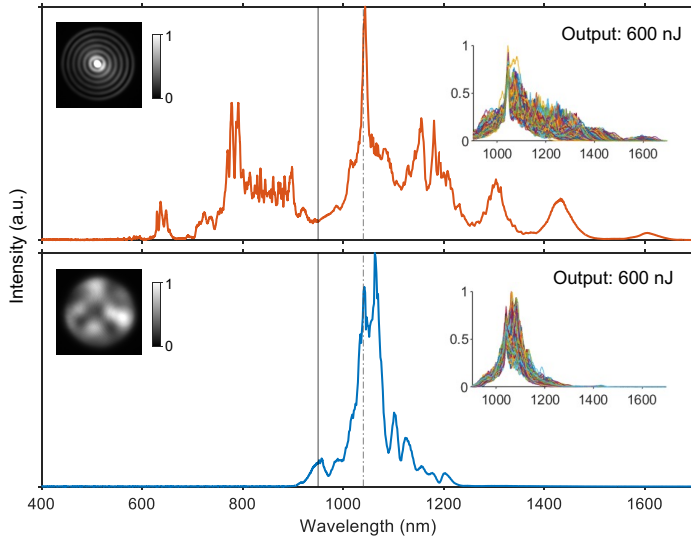


**Fig. 6** Extension of fiber shaper to an input wavelength of 1040 nm. 220-fs pulses were launched into the same standard silica SI MMF (50/125  $\mu\text{m}$ , 0.22 NA) with a length of 30 cm. Normalized intensity patterns in gray scale represent the near-fields of the fiber output at low-power levels, indicating  $\text{LP}_{07}$  and a mixture of lower-order modes were excited in the two cases, respectively. Output energy was fixed to 600 nJ. Inset shows the spectral tunability between 900 nm and 1700 nm, obtained with 1000 different fiber shape configurations. Vertical solid lines mark the spectral range measured by different spectrometers. The dash-dotted line denotes the input wavelength.

### 3 Discussion

In summary, we have presented a new way of controlling nonlinear effects by leveraging both the spatial and temporal degrees of freedom of the multimodal pulse propagation through a programmable fiber shaper. This method unlocks access to an even higher-dimensional space of spatiotemporal dynamics and two-octave-wide high peak power in an off-the-shelf SI MMF. The major contributions of this work include (1) opening up novel perspectives for spatiotemporal control of nonlinear multimode pulse propagation, (2) proposing an avenue for power scaling and field control of broadband sources from visible to NIR-IR regime, and (3) providing accessible control designs that can be rapidly adopted for both nonlinear and linear modulation of multimode fibers.

Our proposed method directly modulates the modal interactions during the pulse temporal evolution using a slip-on 3D-printed fiber shaper, without

additional non-fiber modulation layers such as free-space SLMs for wavefront shaping in spatial and temporal domains. The all-fiber route to single-stage nonlinear conversion inherently contributes to strong alignment robustness, great long-term stability (see Fig. 8), and high spectral band energy. The fiber shaper excels in modulating the multimodal pulse propagation, which SLM cannot access easily. However, it is worth noting the SLM excels in modulating the input, which the fiber shaper cannot access easily (e.g., the broadening shown in Fig. 6). Because of the distinction of the modulation domains, these two approaches are complementary and can be implemented together to maximize control degrees of freedom.

Compared to the commonly used GRIN MMFs, the higher damage threshold and the significantly higher tunability of SI MMFs make it an essential part of the unprecedented spatiotemporal control of the high-power multimodal nonlinear effects. As a result, the proposed apparatus leads to a fiber source with great tunability in spectral (up to 166-fold reallocation), temporal (up to 4-fold shortening), and spatial domains. Furthermore, the fiber shaper enables combined spectral and temporal tuning, leading to high peak power levels across two-octave spectral bands. For instance, at  $750\pm 25$  nm, the peak power reached 0.72 MW and 0.15 MW at  $1225\pm 25$  nm, surpassing the expected regime of operation, which is usually the soliton regime for its inherently high spectral density and short pulse duration.

These performances (1) overcome the bandwidth limitation of existing high-peak-power fiber sources based on soliton formation (12, 32, 82–84) and (2) demonstrate orders of magnitude higher peak power compared to existing tunable fiber-based broadband sources (85). These properties could benefit the emerging but technologically demanding applications in optical sensing, imaging, manipulation, and computing, that require light sources with broad spectral coverage, great tunability, ultrafast pulses (femtosecond-level pulse duration), stability, and/or high spectral density of energy and peak power.

## 4 Methods

### 4.1 Experimental setups and measurements

Pulses with an energy up to 800 nJ and duration of 40–60 fs were launched into 30-cm-long MMFs that were mounted on a three-axis translation stage, with the slip-on fiber shaper placed closely thereafter. This length of the fiber allows for effective spectral tuning without significantly dispersing pulses due to an unnecessarily long fiber. A 6-cm doublet was used to form a 16- $\mu$ m ( $1/e^2$  radius) focal spot on the input facet of the MMFs, resulting in a coupling efficiency of 85%. Two types of MMFs of the same core sizes were tested, namely the silica-core SI MMF (Thorlabs FG050LGA) and GRIN MMF (Corning OM4). The pulses out of the MMFs were split twice to couple into three different grating spectrometers after passing individual optical diffusers. The diffusers were used to reduce the spatial variance of the spectra out of

MMFs. Each of these spectrometers covers a specific wavelength range: 192–1020 nm (Thorlabs CCS200), 899–1702 nm (Ocean Insight NIRQuest+1.7), and 858–2573 nm (Ocean Optics NIR256-2.5). To combine the three spectra obtained from the individual spectrometers, we selected 950 nm and 1600 nm as the reference points for “stitching”. For each spectral region separated by these reference points, we first subtracted the background noises measured when the optical signals were blocked, then multiplied a scaling factor to the spectral traces to align their overall heights with those of the neighboring region at the stitching point. The pulse duration was measured using an intensity autocorrelator (APE PulseScope) based on the second-harmonic generation detection. The near-field beam profiles were acquired by two cameras. A CMOS-based (Mako G-040B) was used for the visible and near-infrared regions, and a thermal imaging camera based on silicon microbolometer (DataRay WinCamD-FIR2-16-HR) was for longer wavelengths above 1700 nm. The optical powers were measured using a thermal power sensor (Thorlabs S425C-L). The fiber output is collimated by a parabolic mirror of 25.4-mm focal length (Edmund Optics 36-586), and then expanded by a pair of 4-f relay systems to slightly overfill the objective’s pupil size (15.12 mm). A dichroic mirror (Thorlabs DMLP650L) is placed before the objective lens, which separates the excitation signals from the emission signals in the detection channels.

## 4.2 Simulations

In all simulations, we assumed a single linear polarization for simplification. The simulated spectra in Fig. 7b were acquired using the GMMNLSE (59):

$$\frac{\partial A_p}{\partial z} = \mathcal{D}\{A_p\} + i \frac{n_2 \omega_0}{c} \left( 1 + \frac{i}{\omega_0} \frac{\partial}{\partial t} \right) \sum_{l,m,n} \left\{ (1-f_R) S_{plmn}^K A_l A_m A_n^* + f_R S_{plmn}^R A_l [h^*(A_m A_n^*)] \right\} \quad (2)$$

implemented with a numerical solver (58) in MATLAB. In the equation above,  $A_p$  is the abbreviation of  $A_p(z, t)$  representing the temporal envelope of the spatial mode- $p$ ;  $\mathcal{D}$  denotes the linear propagation including dispersion effects.  $S_{plmn}^K$  and  $S_{plmn}^R$  are the mode overlap factors responsible to the instantaneous Kerr effect and Raman effect, determined by the spatial overlap of the four spatial modes involved. We set the nonlinear index  $n_2 = 2.3 \times 10^{-20} \text{ m}^2/\text{W}$  and the Raman contribution  $f_R = 0.18$ ; we included the self-steepening effect and up to the fourth-order linear dispersion effects. The mode and dispersion parameters of the SI MMF were calculated based on its pure silica core and its NA of 0.22.



The linear coupling coefficient  $Q_{np}$  in equation (1) and Fig. 3e,j was calculated as

$$Q_{np} = \frac{k_0}{2n_{\text{eff}}} \iint \varepsilon_0 [n^2(x, y) - n_0^2(x, y)] F_n(x, y) F_p^*(x, y), \quad (3)$$

where the scalar function  $F(x, y)$  represents the transverse fiber mode profile (see Fig. 3c,h). The mode parameters of the GRIN MMF were calculated based on a standard telecommunication-grade parabolic GRIN fiber used in (58).

### 4.3 Fiber shaper design

To generate precisely controlled macro-bending to the fiber, we designed a device called fiber shaper. This device was fabricated using 3D printing (Stratasys Fortus 380mc) with acrylonitrile styrene acrylate material. The fiber shaper features a rectangular base with five slots that can hold the translating units (referred to as actuators in Fig. 1a) and constrain their linear motion in the desired direction. Each translating unit is powered by its own stepper motor (ELEGOO 28BYJ-48) through a 3D-printed rack and pinion system, allowing for individual control over their linear motion through a microcontroller (ELEGOO Mega R3) that communicates with a computer. To mount the fiber onto each translating unit, it is passed through a 0.5-mm-wide gap created by two disks and secured in place with a square cap. This design minimizes tension on the fiber during bending, and two half-disks with securing caps at the entrance and exit of the device ensure optimal functionality. The radius of the disk, which determines the minimum bend radius the fiber shaper can apply, is designed to be 10 mm to minimize bending-induced transmission loss. Different device parameters were tested to optimize the spectral tunability of the fiber shaper (see Section 9.2 and Figs. 10–12). As a result, the rich combinations of actuator translation displacements create a vast array of fiber shape configurations, allowing for effective utilization of the spatial and temporal degrees of freedom in controlling nonlinear pulse propagation in SI MMFs with high light throughput.

### 4.4 Multiphoton microscopy

The multiphoton microscopy images were acquired using a custom-built inverted scanning microscope. The microscope used a pair of galvanometer mirrors (ScannerMAX Saturn-5 Galvo and Saturn-9 Galvo) to scan the beam. The beam was then focused by a water immersion objective (Olympus XLPLN25XWMP2, 1.05 NA). The emitted photons were collected using a photomultiplier (Thorlabs PMT2101). During imaging, the fiber source was pumped by 800 nJ 46 fs pulses at 1300 nm and 1 MHz repetition rate. The repetition rate of the OPA (Light Conversion Cronus-3P) was also fixed to 1 MHz during imaging. Fluorescent carboxyl polystyrene (Bangs Laboratories Inc FCDG009) was used as the imaging sample for characterization, a proper emission filter (Edmund Optics  $530 \pm 22.5$  nm) was chosen to match

its fluorescence emission spectrum. Fixed tissue from the mouse whisker pad was used in label-free imaging, where emission filters (Semrock  $609\pm 28.5$  nm, Edmund Optics  $530\pm 22.5$  nm, Thorlabs  $405\pm 5$  nm) were chosen for collecting the SHG, 3PAF, and THG signals, respectively. Raw images were loaded onto FIJI (National Institutes of Health) to apply pseudo-color maps. The bead sample images with 750 nm, 1225 nm, and 1300 nm excitation were respectively acquired with pixel dwelling times of 6  $\mu$ s, 6  $\mu$ s, and 10  $\mu$ s, all with 150- $\mu$ m field of view. The tissue sample images were acquired with a 30- $\mu$ s pixel dwelling time and a 900- $\mu$ m field of view, and  $4\times 4$  images were stitched to represent the mosaicked image. The greedy search method was implemented with the imaging signals as feedback. Specifically, the displacement of each actuator on the fiber shaper was sequentially chosen with the imaging signals maximized.

To calculate the signals of the bead sample images, we selected a few random regions of interest (ROI), each of which contained a spherical bead. The signals from measurement were calculated as the sum of pixel values within the ROIs. The theoretical value of the signals was determined by the multiphoton fluorescence generation efficiency based solely on pulse energy and duration as

$$S_n = C_n \frac{E_p^n}{\tau_p^{n-1}} \quad (n = 2, 3), \quad (4)$$

where  $S_n$  refers to the  $n$ -photon generation efficiency,  $C_n$  is the corresponding constant coefficient,  $E_p$  and  $\tau_p$  refer to the pulse energy and duration, respectively (see Section 9.3).

## 5 Data availability

The data that support the findings of this study are available from the corresponding author upon reasonable request and through collaborative investigations.

## 6 Code availability

The codes that support the findings of this study are available from the corresponding author upon reasonable request and through collaborative investigations.

## 7 Acknowledgement

The work has been supported by MIT startup funds. H.C. acknowledges support from the MIT Kailath Fellowship. K.L. acknowledges support from the MIT Jacobs Presidential. We thank Peter So for sharing with us their lab space and lasers during lab renovation, James Fujimoto for loaning the optical spectrum analyzer, and Phillip Keathley for loaning the autocorrelator and thermal camera. We would like to express our sincere gratitude to them and their students Matthew Yeung, and Lu-Ting Chou for valuable insights on

nonlinear optics. We also extend our appreciation to Kristina Monakhova from our lab for providing constructive comments on the manuscript that greatly improved its clarity and quality. Our appreciation also goes to Miaomiao Jin from McGovern Institute for helping provide the tissue samples for our imaging experiments.

## 8 Author contributions

T.Q., H.C., and S.Y. conceived the idea of the project. S.Y. supervised the research and obtained the funding. T.Q., H.C., and K.L. built the optical setup and performed the experiments and simulations. M.L., E.L., and F.W. provided and prepared the tissue samples. T.Q., H.C., K.L., L.Y., and S.Y. wrote the manuscript with the input from all authors.

## 9 Supplementary

### 9.1 Supplementary Note 1. Multimodal nonlinear pulse propagation and spectral broadening in the SI MMF

To gain insights into the broadening and the tuning mechanisms, we first investigated the evolution of the output spectra with gradually increasing input pulse energy by using the characterization setup as depicted in Fig. 2. The fiber shaper was set to its initial state with no bending applied to the fiber. The results are presented in Fig. 7a. As the injected pulse energy gradually increases, SPM, XPM, and intermodal FWM begin to dominate the spectral broadening process. As the input energy increases further, the output spectrum extends to the anomalous dispersion regime and multimode solitons (i.e., solitary waves consisting of multiple spatial modes) begin to form, due to the balancing between the nonlinear phase modulation and dispersive effects including the intramodal group velocity dispersion and intermodal velocity mismatch (51). Meanwhile, excess energy from the soliton fission process is emitted as dispersive waves through the interaction between the nonlinear and higher-order dispersion effects. The dispersive waves are generated at shorter wavelengths to satisfy the phase-matching condition (50). With further increase in input energy, the multimode soliton undergoes a redshift, resembling soliton self-frequency shifting (37), and eventually the spectrum extends beyond the near-infrared-II region. Accordingly, the phase-matched dispersive waves shift towards the visible region. These observations are in agreement with the findings reported in (49, 50, 52) with input wavelengths deeper into the anomalous dispersion regime.

In addition, the fiber output power at 800-nJ input pulse energy was monitored for 1 hour to assess its stability (Fig. 8), which was measured to reflect 1–2% fluctuations at different wavelengths. Despite exceeding the critical power for catastrophic self-focusing (about 8 MW for silica at 1300 nm (86)), the pronounced dispersion effects associated with ultrashort pulses can effectively modify the dynamics of self-focusing, thereby preventing the exponential

increase in peak intensity (87). In this study, the fiber source was stable enough to generate reproducible output modulation and biological images (see later sections). Nevertheless, the fluctuation metric could potentially be improved by using a better power meter (low dynamic range was used for the wavelength range above 1100 nm in this study), a more environmentally controlled optical space (temperature and humidity), and a more isolated fiber configuration (gel or air isolation).

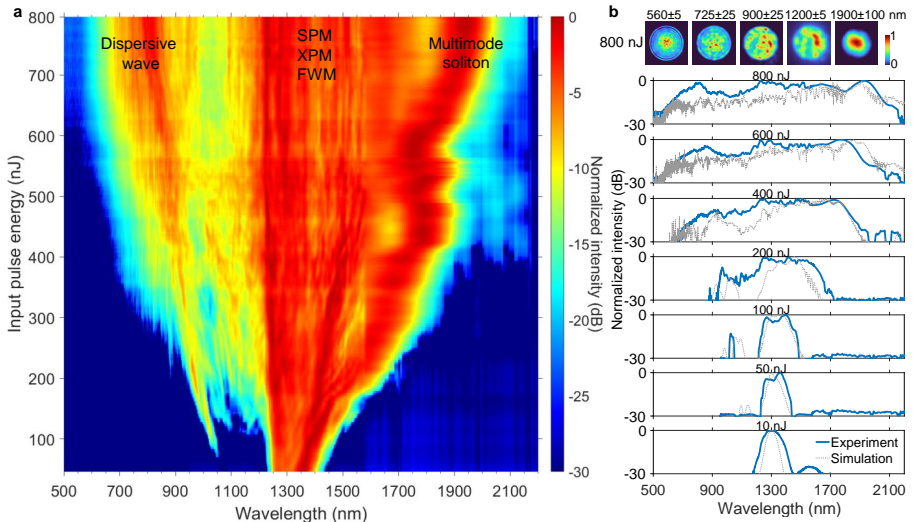


**Fig. 7 Multimodal spectral broadening in SI MMF.** **a**, Spectral evolution as a function of increasing input pulse energy in a 30-cm-long SI MMF, showing the emergence of three spectral windows dominated by distinct nonlinear effects. **b**, Output spectra at selected input pulse energies. The top row presents the spectrally filtered near-field beam profiles at an input energy of 800 nJ, numbers above each profile denote the center wavelength and bandwidth of the bandpass filter applied. Numerical simulations are presented in dotted gray, with the seven modes assumed to be excited with equal energy and phase. For visualization purposes, the spectrum and beam profile at each input pulse energy are normalized to their respective peak values at that energy.

To validate our experimental results, we performed numerical simulations (Fig. 7b) using the simplified (1+1)D model based on the generalized multimode nonlinear Schrödinger equation (GMMNLSE) (58, 59) (see Methods) with the same fiber parameters and launching conditions as in the experiments. Only the first seven radially symmetric modes are included to save computation time. Overall, we observed a good agreement in the spectral broadening between the experimental and numerical results at all energy levels. The discrepancy in the distribution of power spectral density is likely due to the limited number of modes in the simulation, which may not fully capture the multimodal nonlinear broadening in experiments.

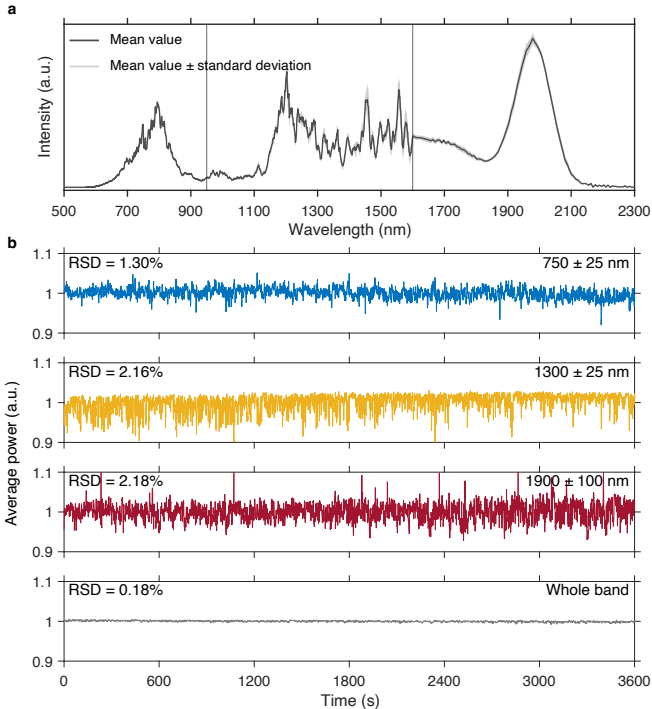


**Fig. 8 Stability of the MMF source.** **a**, Spectral stability of the SI MMF source obtained from the output spectra recorded per second for a period of 1 hour. The solid black trace represents the mean value, and the surrounding gray region indicates the level of variation (quantified by the standard deviation) of the recorded spectra. **b**, Normalized output average power of the SI MMF source recorded per second for a period of 1 hour. A silicon-based photodiode sensor (Thorlabs PM16-130) was used to measure the optical power at wavelength below 1100 nm and a thermal power sensor (Thorlabs S425C-L) was used to measure the optical power of longer wavelengths and the whole band. The SI MMF was pumped by 800-nJ 46-fs pulses at 1300 nm. RSD: relative standard deviation.

## 9.2 Supplementary Note 2. Optimization of the fiber shaper device

The fiber shaper enables spatiotemporal control of the nonlinear effects in SI MMFs, underlying great tunability in the fiber source properties to adapt to diverse applications. To maximize this tunability, we investigate several key parameters involved in the design of the fiber shaper. These parameters include the number of actuators, as well as the total range and resolution of the actuator’s linear motion. The impact of these parameters on the 900–1700 nm band are shown in Figs. 10–12, where we define an average spectral tuning ratio ( $\eta$ ) to quantify the tunability:

$$\eta = \frac{1}{N} \sum_{n=1}^N \frac{I_{\lambda_n}^{\max}}{I_{\lambda_n}^{\min}}. \quad (5)$$

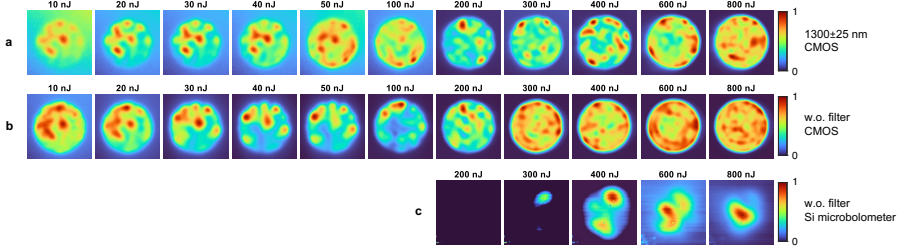


**Fig. 9 Multimodal spectral broadening in SI MMF.** **a–c**, Representative results of near-field beam profiles out of a 30-cm-long SI MMF at different input pulse energies (1300 nm input wavelength) acquired using a CMOS camera (Mako, G-040B) with **(a)** and without **(b)** a bandpass filter; and a thermal imaging camera based on silicon (Si) microbolometer (DataRay, WinCamD-FIR2-16-HR) with no bandpass filter applied **(c)**.

$N$  denotes the number of discrete wavelengths acquired by the spectrometers,  $I_{\lambda_n}^{\max}$  and  $I_{\lambda_n}^{\min}$  refer to the maximum and minimum intensity at each wavelength. Our results indicate that the performance is optimized when using 5 actuators, a displacement range of 20 mm, and an actuator motion resolution of 5 mm. Notably, these parameters are specifically tailored to this device and may require adjustments for devices with different physical dimensions.

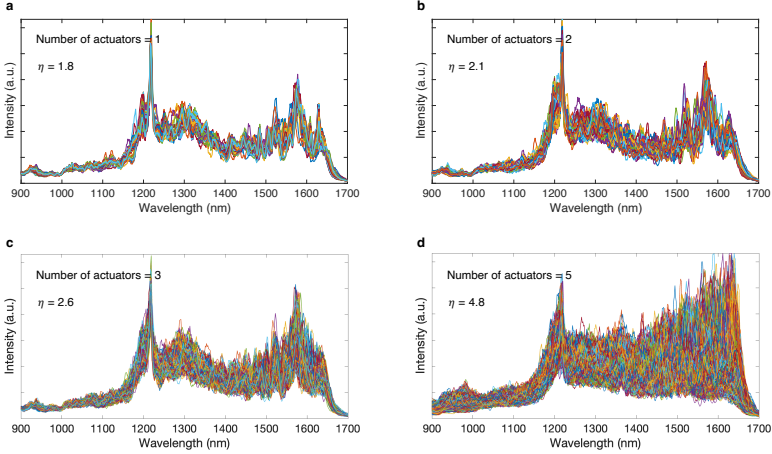


**Fig. 10 Spectral tunability of the fiber shaper with different numbers of actuators.** **a–d**, The output spectra of the fiber-shaper-controlled SI MMF with 1 **(a)**, 2 **(b)**, 3 **(c)**, and 5 **(d)** actuators, respectively. The input wavelength is set at 1300 nm.

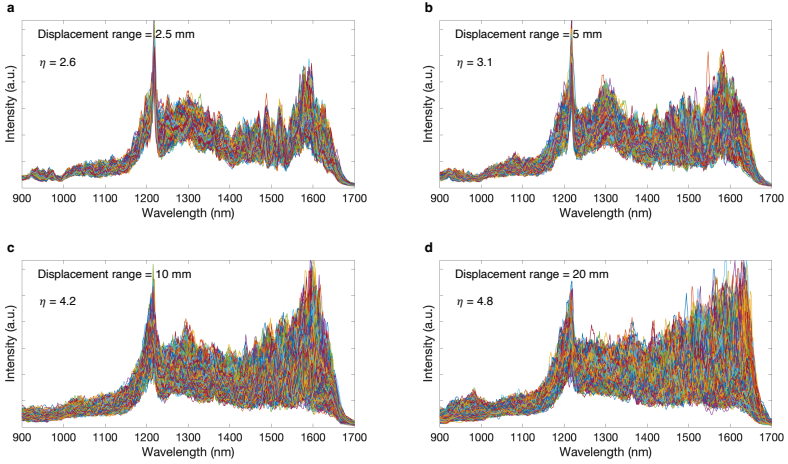


**Fig. 11 Spectral tunability of the fiber shaper with different displacement ranges.** a–d, The output spectra of the fiber-shaper-controlled MMF with a displacement range of 2.5 mm (a), 5 mm (b), 10 mm (c), and 20 mm (d), respectively, all with 5 actuators and a motion resolution of 5 mm. The input wavelength is set at 1300 nm.

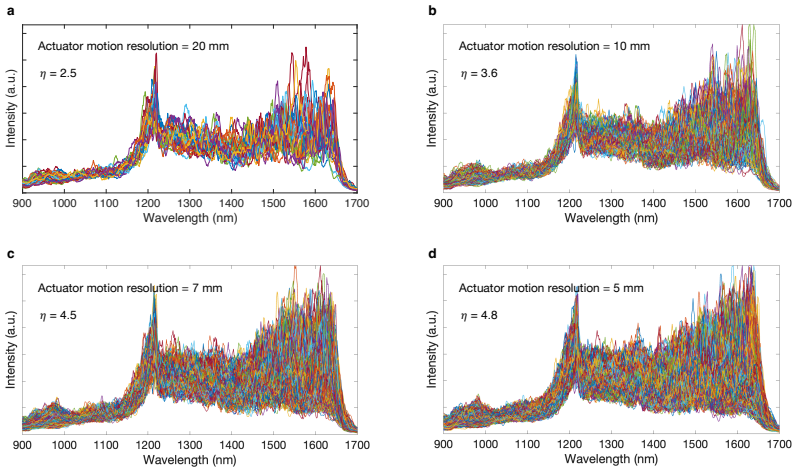


**Fig. 12 Spectral tunability of the fiber shaper with different actuator motion resolutions.** a–d, The output spectra of the fiber-shaper-controlled SI MMF with the actuator motion resolution set at 20 mm (a), 10 mm (b), 7 mm (c), and 5 mm (d), respectively, all with 5 actuators and a displacement range of 20 mm. The input wavelength is set at 1300 nm.

### 9.3 Supplementary Note 3. Derivation of the multiphoton generation efficiency using a fiber source

The derivation follows one of the foundational references of two-photon fluorescence (2PF) imaging (88). The motivation of this derivation is to provide insights into how the multiphoton signal was optimized through fiber-shaper-assisted temporal and spectral shaping of the pulse.

Given the same sample, we consider how the properties of the excitation source would affect the  $n$ -photon generation efficiency, which is described by the time-averaged fluorescence photon fluxes  $S_n = \langle S_n(t) \rangle$ . Since we assume only the excitation source varies, we can express  $S_n(t)$  solely in terms of the intensity of the excitation  $I(\mathbf{r}, t)$ , that

$$S_n(t) \propto \int_V dV I^n(\mathbf{r}, t), \quad (6)$$

where  $V$  is the illuminated volume. We then express  $I(\mathbf{r}, t)$  as  $I(\mathbf{r}, t) = I_0(t)F(\mathbf{r})$  to further separate the temporal and spatial properties of the source, where  $I_0(t)$  is the temporal distribution of the excitation source intensity and  $F(\mathbf{r})$  is the normalized spatial distribution. Substitute it back to equation (6), we have

$$S_n \propto g^{(n)} \langle I_0(t) \rangle^n \int_V dV F^n(\mathbf{r}), \quad (7)$$

where  $g^{(n)} = \langle I_0^n(t) \rangle / \langle I_0(t) \rangle^n$  is the  $n$ -th order temporal coherence. In this work, the repetition rate (1 MHz) is the same for both the laser source and the MMF source, we therefore can further express the temporal term using the pulse energy  $E_p$ , pulse duration  $\tau_p$ , and  $g_p^{(n)}$  that only depends on the pulse shape:

$$g^{(n)} \propto \frac{g_p^{(n)}}{\tau_p^{n-1}}, \quad \langle I_0(t) \rangle \propto E_p. \quad (8)$$

Finally, using the normalized PSF of the source to represent  $F(\mathbf{r})$ , we arrive at

$$S_n \propto \frac{g_p^{(n)} E_p^n}{\tau_p^{n-1}} \int dV \text{PSF}^n(\mathbf{r}). \quad (9)$$

Equation (9) implies that the properties of a source that would affect the multiphoton generation efficiency are: the pulse energy  $E_p$ , the pulse duration  $\tau_p$ , the PSF distribution  $\text{PSF}(\mathbf{r})$ , and the factor  $g_p^{(n)}$  related to the pulse shape. In the imaging section, we simplify the model by assuming different sources share the same  $g_p^{(n)}$  and  $\text{PSF}(\mathbf{r})$ . As a result, the fiber shaper optimization (i.e., finding the optimal actuator configuration  $s \in \mathcal{S}$ ) can be formulated as

$$\max_{s \in \mathcal{S}} \frac{E_p^n(s; \lambda)}{\tau_p^{n-1}(s; \lambda)}, \quad (10)$$



where  $\mathcal{S}$  is the space of all configurations.

Although not accounted for in the formulation, we observed that PSF can also be more confined with fiber shaper optimization. More advanced optimization scheme will be useful to further improve the spectral-temporal-spatial customization of the fiber source to push the fiber shaper to its limit.

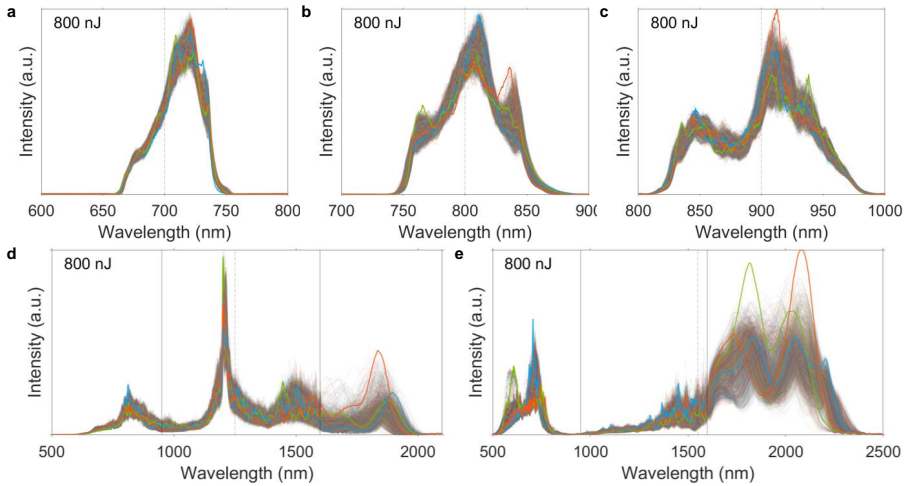


**Fig. 13 Fiber-shaper-controlled SI MMF with other input wavelengths.** a–e, Spectral broadening and tunability of varied input wavelengths of 700 nm (a), 800 nm (b), 900 nm (c), 1250 nm (d), and 1550 nm (e) in the same 30-cm-long fiber, with fixed input pulse energy of 800 nJ and the same set of macro-bending applied. Three representative spectra corresponding to three randomly chosen configurations are highlighted in distinct colors. Vertical solid lines mark the spectral range measured by different spectrometers. The dash-dotted line denotes the input wavelength.

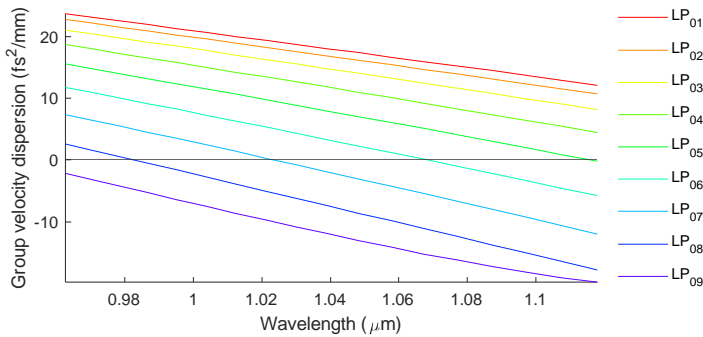


**Fig. 14 Shifted zero-dispersion wavelengths of the higher-order modes.**

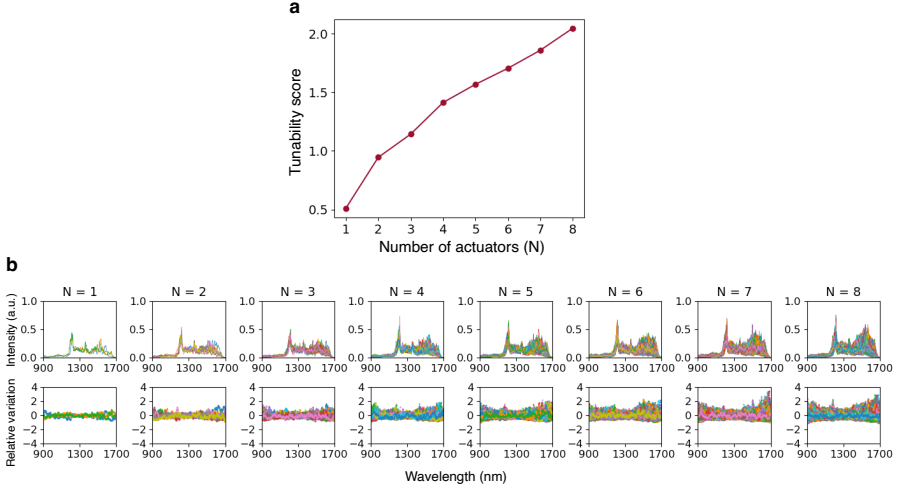


**Fig. 15 Spectral tunability with respect to the number of actuators.** **a**, The relationship between spectral tunability and the number of actuators. The tunability score is quantified by the mean spectral tuning range across the entire wavelength spectrum  $\frac{1}{N} \sum_i [(I_{\lambda_i}^{\max} - I_{\lambda_i}^{\min}) / \bar{I}_{\lambda_i}]$ . **b**, All spectral data and the relative intensity variation at each wavelength  $(I_{\lambda_i} - \bar{I}_{\lambda_i}) / \bar{I}_{\lambda_i}$ .

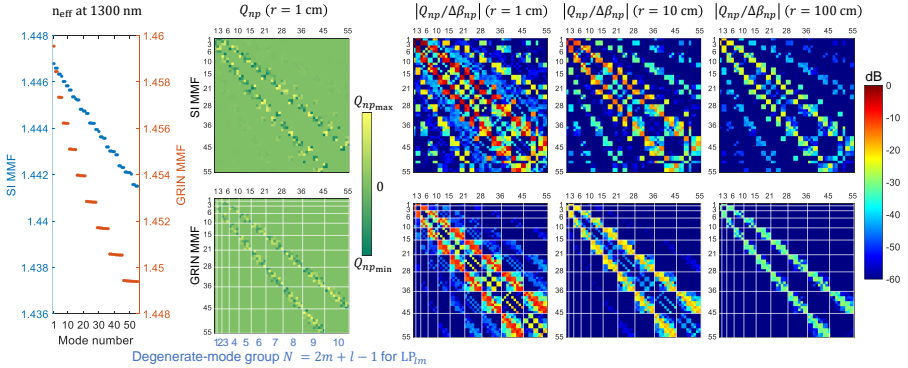


**Fig. 16 Simulation results of bending-induced mode coupling in step-index (SI) and gradient-index (GRIN) multimode fibers (MMFs).** The first two columns show the effective refractive index  $n_{\text{eff}}$  and the coupling coefficients  $Q_{np}$  for the first 55 spatial modes of the SI and GRIN MMFs. The right panel shows the linear mode coupling strength  $|\frac{Q_{np}}{\Delta\beta_{np}}|$  (89) resulting from macro-bending at various bending radii (1 cm, 10 cm, and 100 cm). Modes in the GRIN MMF are clustered as the degenerate-mode group, indicated by the solid white lines.

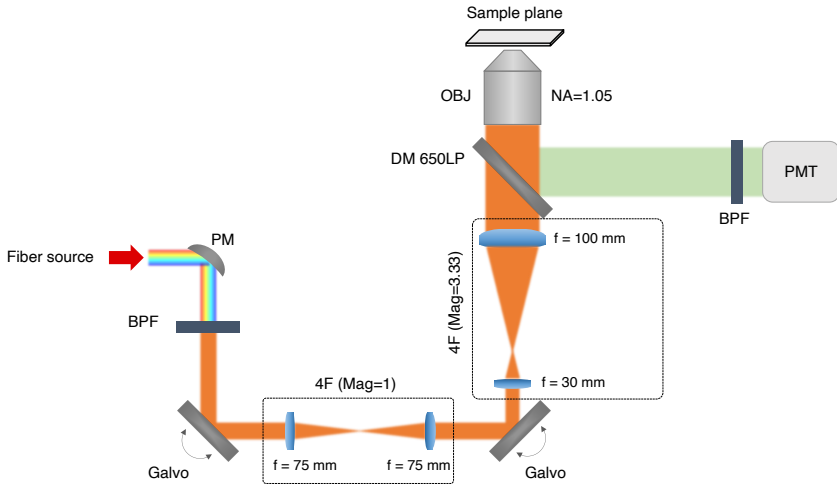


**Fig. 17 Schematic of the multiphoton imaging setup.** PM: parabolic mirror; BPF: bandpass filter; DM: dichroic mirror; LP: long pass; OBJ: objective lens; PMT: photomultiplier tube.

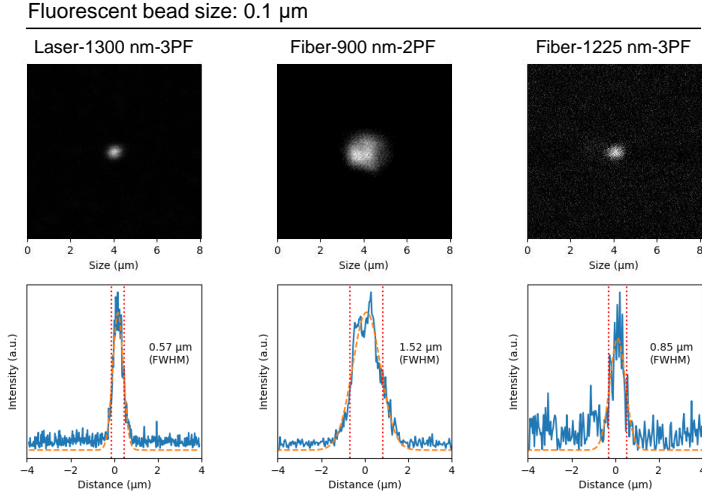


**Fig. 18** PSF measurement of the 3PF excitation with the laser (reference) and the 2PF and 3PF excitation with the fiber source. The size of the bead is 0.1  $\mu\text{m}$ .

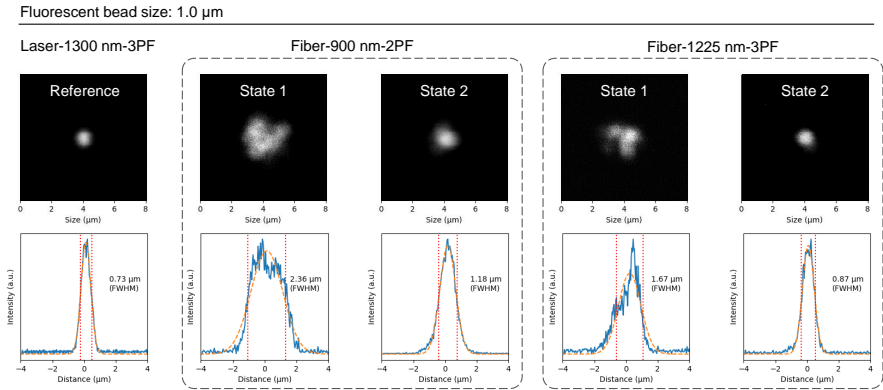


**Fig. 19** Qualitative PSF comparison of the 2PF excitation (900 nm) and the 3PF excitation (1300 nm) with the fiber source under random bending conditions induced by the fiber shaper's different states. The size of the bead is 1  $\mu\text{m}$ .

## References

1. Wright, L. G., Renninger, W. H., Christodoulides, D. N. & Wise, F. W. Nonlinear multimode photonics: nonlinear optics with many degrees of freedom. *Optica* **9**, 824–841 (2022).
2. Krupa, K. *et al.* Multimode nonlinear fiber optics, a spatiotemporal avenue. *APL Photonics* **4**, 110901 (2019).

3. Wright, L. G., Wu, F. O., Christodoulides, D. N. & Wise, F. W. Physics of highly multimode nonlinear optical systems. *Nature Physics* **18**, 1018–1030 (2022).
4. Krupa, K. *et al.* Observation of geometric parametric instability induced by the periodic spatial self-imaging of multimode waves. *Physical review letters* **116**, 183901 (2016).
5. Krupa, K. *et al.* Spatiotemporal light-beam compression from nonlinear mode coupling. *Physical Review A* **97**, 043836 (2018).
6. Leventoux, Y. *et al.* 3d time-domain beam mapping for studying nonlinear dynamics in multimode optical fibers. *Optics Letters* **46**, 66–69 (2021).
7. Shalaby, B. *et al.* Visible supercontinuum generation by dual-wavelength pumping in multimode rectangular optical fibers. In *2014 Conference on Lasers and Electro-Optics (CLEO)-Laser Science to Photonic Applications*, 1–2 (IEEE, 2014).
8. Zhou, R., Ren, J., Lou, S., Ju, Y. & Wang, Y. Half mj supercontinuum generation in a telecommunication multimode fiber by a q-switched tm<sub>0</sub> laser. *Journal of the Optical Society of Korea* **19**, 7–12 (2015).
9. Lopez-Galmiche, G. *et al.* Visible supercontinuum generation in a graded index multimode fiber pumped at 1064 nm. *Optics Letters* **41**, 2553–2556 (2016).
10. Krupa, K. *et al.* Spatiotemporal characterization of supercontinuum extending from the visible to the mid-infrared in a multimode graded-index optical fiber. *Optics Letters* **41**, 5785–5788 (2016).
11. Eftekhari, M. A. *et al.* Versatile supercontinuum generation in parabolic multimode optical fibers. *Optics Express* **25**, 9078–9087 (2017).
12. Rishøj, L., Tai, B., Kristensen, P. & Ramachandran, S. Soliton self-mode conversion: revisiting raman scattering of ultrashort pulses. *Optica* **6**, 304–308 (2019).
13. Wright, L. G., Christodoulides, D. N. & Wise, F. W. Spatiotemporal mode-locking in multimode fiber lasers. *Science* **358**, 94–97 (2017).
14. Teğin, U., Kakkava, E., Rahmani, B., Psaltis, D. & Moser, C. Spatiotemporal self-similar fiber laser. *Optica* **6**, 1412–1415 (2019).
15. Wei, X., Jing, J. C., Shen, Y. & Wang, L. V. Harnessing a multi-dimensional fibre laser using genetic wavefront shaping. *Light: Science & Applications* **9**, 149 (2020).

16. Ding, Y. *et al.* Spatiotemporal mode-locking in lasers with large modal dispersion. *Physical Review Letters* **126**, 093901 (2021).
17. Xiong, W. *et al.* Spatiotemporal control of light transmission through a multimode fiber with strong mode coupling. *Physical review letters* **117**, 053901 (2016).
18. Vaughan, J. C., Feurer, T. & Nelson, K. A. Automated two-dimensional femtosecond pulse shaping. *JOSA B* **19**, 2489–2495 (2002).
19. Demas, J. *et al.* Intermodal nonlinear mixing with bessel beams in optical fiber. *Optica* **2**, 14–17 (2015).
20. Nazemosadat, E., Pourbeyram, H. & Mafi, A. Phase matching for spontaneous frequency conversion via four-wave mixing in graded-index multimode optical fibers. *JOSA B* **33**, 144–150 (2016).
21. Eslami, Z. *et al.* Two octave supercontinuum generation in a non-silica graded-index multimode fiber. *Nature Communications* **13**, 2126 (2022).
22. Redding, B., Popoff, S. M. & Cao, H. All-fiber spectrometer based on speckle pattern reconstruction. *Optics express* **21**, 6584–6600 (2013).
23. Xiong, W. *et al.* Deep learning of ultrafast pulses with a multimode fiber. *APL Photonics* **5**, 096106 (2020).
24. Xu, C. & Wise, F. Recent advances in fibre lasers for nonlinear microscopy. *Nature photonics* **7**, 875–882 (2013).
25. Moussa, N. O. *et al.* Spatiotemporal beam self-cleaning for high-resolution nonlinear fluorescence imaging with multimode fiber. *Scientific Reports* **11**, 18240 (2021).
26. Berti, N. *et al.* Interplay of thermalization and strong disorder: Wave turbulence theory, numerical simulations, and experiments in multimode optical fibers. *Physical Review Letters* **129**, 063901 (2022).
27. Picozzi, A. *et al.* Optical wave turbulence: Towards a unified nonequilibrium thermodynamic formulation of statistical nonlinear optics. *Physics Reports* **542**, 1–132 (2014).
28. Garnier, J. *et al.* Wave condensation with weak disorder versus beam self-cleaning in multimode fibers. *Physical Review A* **100**, 053835 (2019).
29. Podivilov, E. V. *et al.* Hydrodynamic 2d turbulence and spatial beam condensation in multimode optical fibers. *Physical review letters* **122**, 103902 (2019).

30. Teğın, U., Yıldırım, M., Oğuz, İ., Moser, C. & Psaltis, D. Scalable optical learning operator. *Nature Computational Science* **1**, 542–549 (2021).
31. Rahmani, B. *et al.* Learning to image and compute with multimode optical fibers. *Nanophotonics* **11**, 1071–1082 (2022).
32. Wright, L. G., Christodoulides, D. N. & Wise, F. W. Controllable spatiotemporal nonlinear effects in multimode fibres. *Nature photonics* **9**, 306–310 (2015).
33. Tzang, O., Caravaca-Aguirre, A. M., Wagner, K. & Piestun, R. Adaptive wavefront shaping for controlling nonlinear multimode interactions in optical fibres. *Nature Photonics* **12**, 368–374 (2018).
34. Deliancourt, E. *et al.* Wavefront shaping for optimized many-mode kerr beam self-cleaning in graded-index multimode fiber. *Optics Express* **27**, 17311–17321 (2019).
35. Teğın, U. *et al.* Controlling spatiotemporal nonlinearities in multimode fibers with deep neural networks. *Appl Photonics* **5**, 030804 (2020).
36. Bender, N., Haig, H., Christodoulides, D. N. & Wise, F. W. Spectral speckle customization. *Optica* **10**, 1260–1268 (2023).
37. Renninger, W. H. & Wise, F. W. Optical solitons in graded-index multimode fibres. *Nature communications* **4**, 1719 (2013).
38. Pourbeyram, H., Agrawal, G. P. & Mafi, A. Stimulated raman scattering cascade spanning the wavelength range of 523 to 1750 nm using a graded-index multimode optical fiber. *Applied Physics Letters* **102**, 201107 (2013).
39. Wright, L. G. *et al.* Self-organized instability in graded-index multimode fibres. *Nature Photonics* **10**, 771–776 (2016).
40. Liu, Z., Wright, L. G., Christodoulides, D. N. & Wise, F. W. Kerr self-cleaning of femtosecond-pulsed beams in graded-index multimode fiber. *Optics Letters* **41**, 3675–3678 (2016).
41. Krupa, K. *et al.* Spatial beam self-cleaning in multimode fibres. *Nature Photonics* **11**, 237–241 (2017).
42. Ahsan, A. S. & Agrawal, G. P. Graded-index solitons in multimode fibers. *Optics Letters* **43**, 3345–3348 (2018).
43. Eftekhari, M. *et al.* Accelerated nonlinear interactions in graded-index multimode fibers. *Nature communications* **10**, 1638 (2019).



44. Regelman, D. V., Segev, Y. & Yosub, S. Method for brightness enhancement and modes manipulation of a multimode optical fiber (2016). US Patent 9,329,416.
45. Golubchik, D., Segev, Y. & Regelman, D. Controlled mode mixing in optical fibers. In *International Conference and Exhibition on Optics and Electro-Optics (OASIS 5)* (2015).
46. Resisi, S., Viernik, Y., Popoff, S. M. & Bromberg, Y. Wavefront shaping in multimode fibers by transmission matrix engineering. *APL Photonics* **5**, 036103 (2020).
47. Finkelstein, Z., Sulimany, K., Resisi, S. & Bromberg, Y. Spectral shaping in a multimode fiber by all-fiber modulation. *APL Photonics* **8**, 036110 (2023).
48. Shekel, R. *et al.* Shaping single photons through multimode optical fibers using mechanical perturbations. *arXiv preprint arXiv:2306.02288* (2023).
49. Wu, Y., Bender, N., Christodoulides, D. N. & Wise, F. W. Highly multimode solitons in step-index optical fiber. *APL Photonics* **8** (2023).
50. Eftekhar, M., Lopez-Aviles, H., Wise, F., Amezcua-Correa, R. & Christodoulides, D. General theory and observation of cherenkov radiation induced by multimode solitons. *Communications Physics* **4**, 137 (2021).
51. Wright, L. G., Renninger, W. H., Christodoulides, D. N. & Wise, F. W. Spatiotemporal dynamics of multimode optical solitons. *Optics Express* **23**, 3492–3506 (2015).
52. Zitelli, M. *et al.* Multimode solitons in step-index fibers. *Optics Express* **30**, 6300–6310 (2022).
53. Snyder, A. W. Coupled-mode theory for optical fibers. *JOSA* **62**, 1267–1277 (1972).
54. Marcuse, D. Coupled mode theory of round optical fibers. *Bell System Technical Journal* **52**, 817–842 (1973).
55. Xiao, Y. *et al.* Theory of intermodal four-wave mixing with random linear mode coupling in few-mode fibers. *Optics Express* **22**, 32039–32059 (2014).
56. Bendahmane, A. *et al.* Seeded intermodal four-wave mixing in a highly multimode fiber. *JOSA B* **35**, 295–301 (2018).
57. Mumtaz, S., Essiambre, R.-J. & Agrawal, G. P. Nonlinear propagation in multimode and multicore fibers: generalization of the manakov equations. *Journal of Lightwave Technology* **31**, 398–406 (2012).

58. Wright, L. G. *et al.* Multimode nonlinear fiber optics: massively parallel numerical solver, tutorial, and outlook. *IEEE Journal of Selected Topics in Quantum Electronics* **24**, 1–16 (2017).
59. Horak, P. & Poletti, F. Multimode nonlinear fibre optics: theory and applications. *Recent progress in optical fiber research* **3** (2012).
60. Yariv, A. Coupled-mode theory for guided-wave optics. *IEEE Journal of Quantum Electronics* **9**, 919–933 (1973).
61. Olshansky, R. Mode coupling effects in graded-index optical fibers. *Applied optics* **14**, 935–945 (1975).
62. Caravaca-Aguirre, A. M. & Piestun, R. Single multimode fiber endoscope. *Optics Express* **25**, 1656–1665 (2017).
63. Flaes, D. E. B. *et al.* Robustness of light-transport processes to bending deformations in graded-index multimode waveguides. *Physical review letters* **120**, 233901 (2018).
64. Cao, H., Čižmár, T., Turtaev, S., Tyc, T. & Rotter, S. Controlling light propagation in multimode fibers for imaging, spectroscopy, and beyond. *Advances in Optics and Photonics* **15**, 524–612 (2023).
65. Carpenter, J., Thomsen, B. C. & Wilkinson, T. D. Degenerate mode-group division multiplexing. *Journal of Lightwave Technology* **30**, 3946–3952 (2012).
66. Ferraro, M. *et al.* Femtosecond nonlinear losses in multimode optical fibers. *Photonics Research* **9**, 2443–2453 (2021).
67. Ferraro, M. *et al.* Multiphoton ionization of standard optical fibers. *Photonics Research* **10**, 1394–1400 (2022).
68. Agrawal, G. P. Invite paper: Self-imaging in multimode graded-index fibers and its impact on the nonlinear phenomena. *Optical Fiber Technology* **50**, 309–316 (2019).
69. Lancry, M., Poumellec, B., Chahid-Er-raji, A., Beresna, M. & Kazansky, P. Dependence of the femtosecond laser refractive index change thresholds on the chemical composition of doped-silica glasses. *Optical Materials Express* **1**, 711–723 (2011).
70. Sun, Y. *et al.* Multimode soliton collisions in graded-index optical fibers. *Optics Express* **30**, 21710–21724 (2022).
71. Perret, S. *et al.* Supercontinuum generation by intermodal four-wave mixing in a step-index few-mode fibre. *Appl Photonics* **4** (2019).

72. Yildirim, M., Sugihara, H., So, P. T. & Sur, M. Functional imaging of visual cortical layers and subplate in awake mice with optimized three-photon microscopy. *Nature communications* **10**, 177 (2019).
73. You, S. *et al.* Intravital imaging by simultaneous label-free autofluorescence-multiharmonic microscopy. *Nature communications* **9**, 2125 (2018).
74. Hoover, E. E. & Squier, J. A. Advances in multiphoton microscopy technology. *Nature photonics* **7**, 93–101 (2013).
75. Huland, D. M. *et al.* Three-photon excited fluorescence imaging of unstained tissue using a grin lens endoscope. *Biomedical Optics Express* **4**, 652–658 (2013).
76. Dong, C.-Y., Koenig, K. & So, P. Characterizing point spread functions of two-photon fluorescence microscopy in turbid medium. *Journal of biomedical optics* **8**, 450–459 (2003).
77. Xu, C. & Webb, W. W. Multiphoton excitation of molecular fluorophores and nonlinear laser microscopy. *Topics in Fluorescence Spectroscopy: Volume 5: Nonlinear and Two-Photon-Induced Fluorescence* 471–540 (2002).
78. Demas, J., Rishøj, L. & Ramachandran, S. Free-space beam shaping for precise control and conversion of modes in optical fiber. *Optics express* **23**, 28531–28545 (2015).
79. Ramsay, J. *et al.* Generation of infrared supercontinuum radiation: spatial mode dispersion and higher-order mode propagation in zblan step-index fibers. *Optics Express* **21**, 10764–10771 (2013).
80. Petersen, C. R. *et al.* Mid-infrared supercontinuum covering the 1.4–13.3  $\mu\text{m}$  molecular fingerprint region using ultra-high na chalcogenide step-index fibre. *Nature Photonics* **8**, 830–834 (2014).
81. Kubat, I. & Bang, O. Multimode supercontinuum generation in chalcogenide glass fibres. *Optics Express* **24**, 2513–2526 (2016).
82. Wang, K. & Xu, C. Tunable high-energy soliton pulse generation from a large-mode-area fiber and its application to third harmonic generation microscopy. *Applied physics letters* **99**, 071112 (2011).
83. Zach, A., Mohseni, M., Polzer, C., Nicholson, J. & Hellerer, T. All-fiber widely tunable ultrafast laser source for multimodal imaging in nonlinear microscopy. *Optics Letters* **44**, 5218–5221 (2019).

84. Rishøj, L., Deng, F., Tai, B., Cheng, J.-X. & Ramachandran, S. Jitter-free, dual-wavelength, ultrashort-pulse, energetic fiber sources using soliton self-mode conversion. *Optics Express* **28**, 4333–4339 (2020).
85. Lefort, C. A review of biomedical multiphoton microscopy and its laser sources. *Journal of physics D: Applied physics* **50**, 423001 (2017).
86. Dubietis, A., Tamošauskas, G., Šuminas, R., Jukna, V. & Couairon, A. Ultrafast supercontinuum generation in bulk condensed media (invited review). *arXiv preprint arXiv:1706.04356* (2017).
87. Gaeta, A. L. Catastrophic collapse of ultrashort pulses. *Physical Review Letters* **84**, 3582 (2000).
88. Xu, C. & Webb, W. W. Measurement of two-photon excitation cross sections of molecular fluorophores with data from 690 to 1050 nm. *JOSA B* **13**, 481–491 (1996).
89. Ho, K.-P., Kahn, J. M., Kaminow, I., Li, T. & Willner, A. Mode coupling and its impact on spatially multiplexed systems. *Optical Fiber Telecommunications VI* **17**, 1386–1392 (2013).